Research Square

Preprints are preliminary reports that have not undergone peer review.
They should not be considered conclusive, used to inform clinical practice,
or referenced by the media as validated information.

Unveiling the Atmospheric Corrosion Behavior of Die-cast AZ91D Magnesium Alloy: From Mechanism to Laboratory-to-Field Test Correlation

Beining Du

Bndu10s@alum.imr.ac.cn

BYD Automotive Industry Co., Ltd

Peng Liang

BYD Automotive Industry Co., Ltd

Zhengyao He

BYD Automotive Industry Co., Ltd

Jinjie Wei

BYD Automotive Industry Co., Ltd

Jing Guo

BYD Automotive Industry Co., Ltd

Article

Keywords: magnesium alloy, proving ground vehicle corrosion test, cyclic corrosion test, filiform corrosion

Posted Date: November 2nd, 2026

DOI: https://doi.org/10.21203/rs.3.rs-11212772/v1

License: This work is licensed under a Creative Commons Attribution 4.0 International License.
Read Full License

Additional Declarations: No competing interests reported.

Unveiling the Atmospheric Corrosion Behavior of Die-cast AZ91D Magnesium Alloy: From Mechanism to Laboratory-to-Field Test Correlation

Abstract: The application of Mg alloy components in automobiles enables significant weight reduction. However, the poor corrosion resistance of Mg alloys remains a critical impediment. Moreover, their corrosion mechanisms and modes are fundamentally different from those of conventional materials such as steel and aluminum. Currently, the automotive industry lacks well-established accelerated corrosion testing and evaluation methodologies specifically tailored for Mg alloys. In this study, the corrosion behavior of die-cast AZ91D Mg alloy was systematically investigated under three distinct exposure conditions, including marine atmosphere, proving ground vehicle corrosion test (PGVCT) and various laboratory corrosion environment. The corrosion performance was evaluated in terms of morphology, weight loss rate, and corrosion depth, based on which the atmospheric corrosion mechanism was elucidated and a laboratory-to-field corrosion test correlation was established for the magnesium alloy. This work provides a critical foundation for developing highly relevant accelerated corrosion test method for Mg alloys used in automotive applications.

Key words: magnesium alloy, proving ground vehicle corrosion test, cyclic corrosion test, filiform corrosion

1 Introduction

Magnesium alloys possess comprehensive advantages such as low density, high specific strength, good damping capacity, excellent castability, and recyclability, making them ideal materials for automotive lightweighting [1,2]. However, their poor corrosion resistance significantly impedes their widespread application in exterior automotive components. Currently, the automotive industry generally lacks standardized corrosion testing and evaluation procedures for Mg alloys at both material and component levels. Moreover, the excessively rapid and non-uniform corrosion of Mg alloys observed under neutral salt spray (NSS) conditions deviates markedly from atmospheric corrosion behavior, whereas proving ground vehicle corrosion tests (PGVCT) incur prohibitively high costs. Therefore, developing highly reproducible accelerated corrosion test methods for Mg alloys is essential to facilitate their implementation in automotive exterior components.

It is well known that the electrochemical corrosion of Mg alloys differs significantly from that of common metals such as Zn, Fe, and Al. The cathodic reaction for the electrochemical corrosion of Zn, Fe, and Al is typically oxygen reduction reaction [3-5]. However, due to the extremely low potential of Mg (-2.37 V_{SHE}), the cathodic process in its corrosion is primarily hydrogen evolution reaction (HER):

$$2H_2O + 2e^- \rightarrow 2OH^- + H_2 \qquad (1)$$

Consequently, the corrosion process of Mg alloys is independent of oxygen concentration in the medium, and and their corrosion behavior follows different rules from those of metals such as Zn, Fe, and Al. Therefore, mechanistic investigations into the corrosion behavior of magnesium alloys in both atmospheric and laboratory environments are required.

Die-cast AZ91D alloy was chosen for this study because it is one of the most promising Mg alloys for automotive applications. By studying its corrosion behavior under marine transportation, (PGVCT) and various laboratory conditions, the corrosion behavior is evaluated and compared from three aspects: corrosion morphology, weight loss rate, and corrosion depth. Based on these results, a correlative relationship was established among the corrosion behavior observed in laboratory, proving ground, and marine atmospheric environments. This work provides a foundation for the development of highly relevant accelerated corrosion test methods for Mg alloys, thereby facilitating their broader application in new energy vehicles.

2 Experimental Methods

2.1 Corrosion tests under marine transportation conditions

AZ91D alloy samples were carried on a ship that sailed from Jiangsu, China, to Belgium. The total duration of the voyage was 82 days. The samples, with dimensions of 45 × 40 × 2.6 mm, were hung on the railings of the deck and cargo hold with insulating ropes, six specimens per location. After the 82-day voyage, the samples were collected and their surface morphology was observed. Corrosion products were cleaned using 200 g/L CrO_3 solution, followed by weight loss and corrosion depth measurements. The corrosion rate of the magnesium alloy calculated from weight loss is given by the following equation:

$$CR_m = \frac{\Delta m \times 365 \times 10^6}{A \times t \times \rho} \qquad (2)$$

Where CR_m represents the corrosion rate determined by weight loss, expressed in μm/y; Δm represents weight loss, expressed in grams (g); A represents the exposed surface area, expressed in square meters (m^2); t represents the exposure time, expressed in years (y); and ρ represents the density of the AZ91D alloy, expressed in g/cm^3.



Fig. 1 Photographs showingAZ91D samples and their placement on the deck and in the cargo hold.

The corrosion depth of AZ91D alloy was measured as follows: After cleaning the corrosion products from the tested samples, at least three representative areas were selected based on the corrosion morphology. Ten corrosion depth measurements were taken in each area. The average and maximum corrosion depths (in μm) were then calculated from all measured data points for each corresponding sample.

2.2 Proving ground vehicle corrosion test (PGVCT)

To simulate the corrosion performance of AZ91D alloy when used as an automotive electric drive housing, AZ91D samples were installed on the chassis area of a test vehicle and subjected to a 12-week PGVCT in Hainan, China. The sample dimensions were 30 × 30 × 2.6 mm. The edges and backside of the samples were sealed with tape, and the exposed surface area was measured using a vernier caliper. The samples were mounted on the fuel tank of the test vehicle chassis, at a height similar to the bottom of the electric drive system, as shown in Figure 2. After PGVCT, the

samples were removed, surface morphology was observed, corrosion products were cleaned, and weight loss and corrosion depth were measured. Three parallel samples were set for the same exposure period.

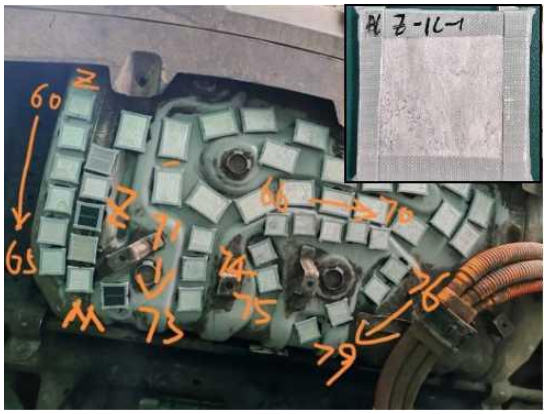


Fig. 2 Photograph showing AZ91D alloy samples mounted on the chassis area of a test vehicle for PGVCT

2.3 Corrosion tests under laboratory conditions

Corrosion behavior of AZ91D alloy were tested NSS and three different cyclic corrosion test (CCT) conditions. The profiles of the three CCT conditions are shown in Figure 3. The sample dimensions were 30 × 30 × 2.6 mm. Edges and backside were sealed with tape, and the exposed surface area was measured. After tests, surface morphology was observed, weight loss and corrosion depth were measured. Three parallel samples were used for each condition.

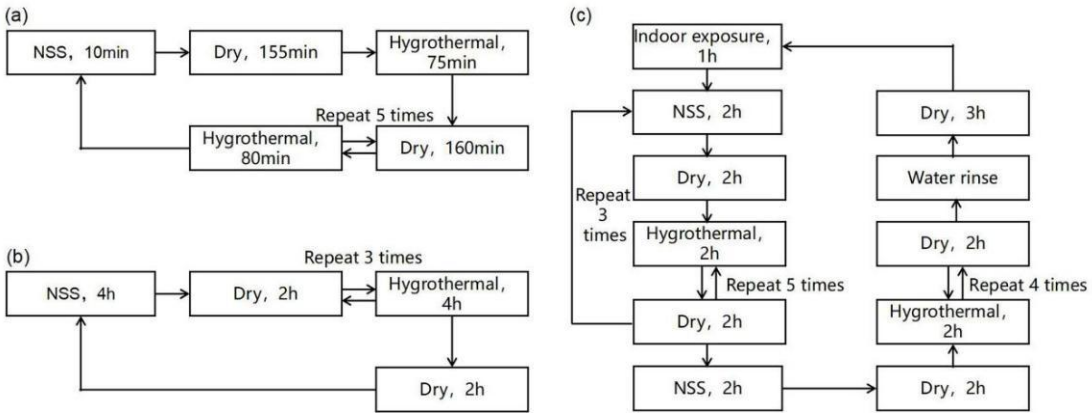


Fig. 3 Profiles of different CCT conditions: (a) CCT 1; (b) CCT 2; (c) CCT 3.

2.4 **Scanning vibrating electrode technique (SVET) experiments**

SVET experiment was conducted through a SVET instrument (VersaSCAN, Princeton, America) to study the filiform corrosion process on AZ91D alloy. AZ91D samples were cut into 15 × 15 × 2.6 mm pieces and mounted in epoxy resin, exposing the 15 × 15 mm face. The sample surface was ground, polished and cleaned, and then immersed in 5% NaCl solution with a conductivity of 57.20 mS/cm. The current density distribution over the same area of the sample surface was detected at different immersion time. A platinum probe with a diameter of 10 μm was chosen to vibrate at an amplitude of 30 μm and a frequency of 80Hz during measurement. The probe scan rate was 50 μm/s. The probe-to-sample distance was controlled around 100 μm. The scan area was 2 × 2 mm dimensions.

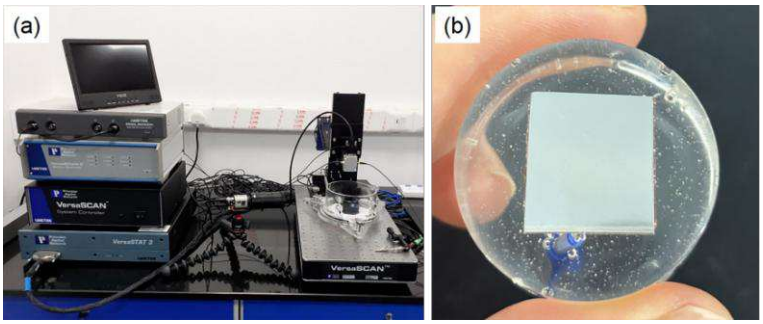


Fig. 4 Photographs showing the SVET equipment and AZ91D alloy sample

2.5 Microstructure observation

The microstructure of AZ91D alloy after corrosion tests was observed using optical microscopy (OM). The samples were sectioned along the longitudinal direction, and the surface was ground, polished, and then etched using 4% HNO_3 + ethanol solution.

3 Experimental Results

3.1 Survey on atmospheric corrosion rate of Mg alloys

According to literature [6-12], the atmospheric corrosion rate of Mg alloys typically ranges from a few to several tens of micrometers per year, and the maximum rate can reach 120 μm/y in coastal regions, as shown in table 1.

Table 1 Atmospheric corrosion rate for Mg alloys

Mg Alloy	Exposure Site	Exposure Duration	Corrosion Rate (μm/y)
AZ31 (rolled)	Wanning, China	5 years	37.6 [6]
AZ61 (wrought)	Wanning, China	2 months	17.07 [7]
	Jiangjin, China		8.477
	Xishuangbanna		6.73
AZ91D (as-cast)	Linfen, China	1 year	10.65 [8]
	Qingdao, China		120
AZ91D (as-cast)	Taiyuan, China	1 year	3.5 [9]
Mg-RE (as-cast)	Qingdao, China	6 months	38.6 [10]
	Beijing, China		28.4
AZ91D (as-cast)	Stockholm, Sweden	1 year	1.8 **[11]**
	Ruda, Sweden		2.2
	Brest, France		4.2
AZ31B (hot extruded)	Shimizu, Japan	1 year	34.6 **[12]**
	Osaka, Japan		26.7

3.2 Corrosion rate of AZ91D alloy during marine transportation

Based on equation (2), the weight-loss corrosion rates for AZ91D alloy samples mounted inside the cabin and on the deck during marine transportation were calculated to be 6 ± 2 μm/y and 90 ± 30 μm/y, respectively. Comparison with the atmospheric corrosion rate in table 1 indicates that the corrosion rate of samples on the deck is higher than that reported in most literature for Mg alloys exposed in coastal regions. This is attributed to the greater seawater deposition on the deck railings of the ship. While the corrosion rate for samples inside the cabin is significantly lower, comparable to rates observed in inland urban areas.

The corrosion morphologies of the samples after marine transportation are shown in Figure 5. After 82-day voyage, the samples mounted on the deck exhibited severe corrosion, with the surface almost entirely covered by corrosion products. After removing the corrosion products, two primary forms of corrosion were observed on the magnesium alloy surface: filiform corrosion and pitting. The depth of filiform corrosion was mostly within 50 μm, while pitting depths could exceed 100 μm. Measurements showed that the average corrosion depth on the deck samples was approximately 80 μm, with a maximum pitting depth of about 200 μm. In contrast, samples from the cabin showed filiform corrosion only in a few small areas, with corrosion depths ranging between 20-60 μm.

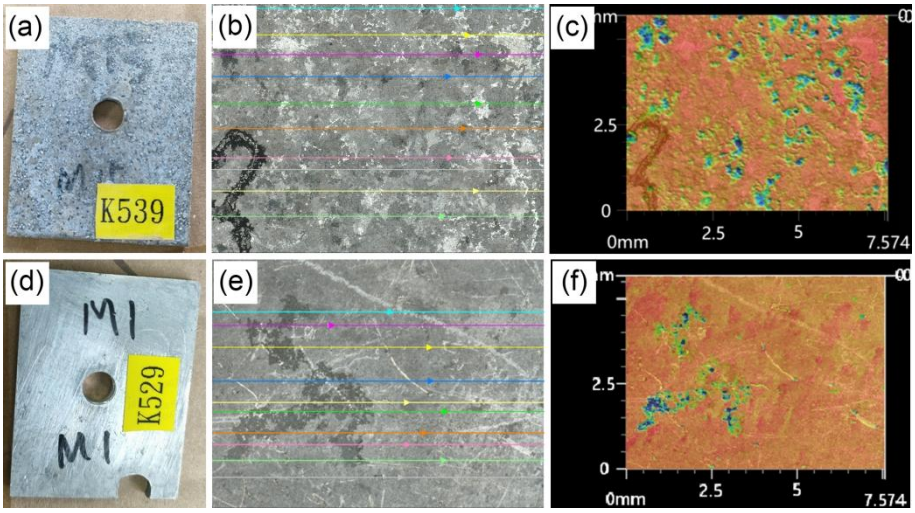


Fig. 5 Corrosion morphology and depth measurements of AZ91D alloy after marine transportation: (a)(b)(c) Samples on the deck; (d)(e)(f) Samples in the cabin

3.3 Corrosion rate of AZ91D alloy under PGVCT

The weight-loss corrosion rate of AZ91D samples mounted on the chassis of a test vehicle was calculated using Equation (2) after PGVCT, and the results are presented in Fig. 6. The corrosion rate decreased progressively with increasing test duration. This is attributed to the protective effect of the accumulating corrosion products, which retarded the corrosion rate in later stages. The average weight-loss rate at 2 weeks was approximately 660 μm/y, decreasing to about 100 μm/y by the final 12-week mark.

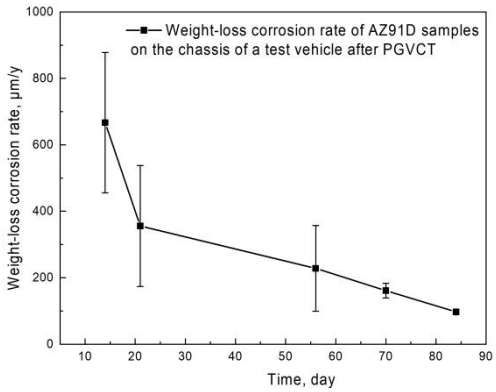


Fig. 6 Weight-loss corrosion rate of AZ91D alloy samples mounted on the chassis during PGVCT

The corrosion morphology evolution during PGVCT were observed (Fig. 7), it can be seen that filiform corrosion appeared on Mg alloy surface at the initial stage. As time progressed, filiform corrosion expanded across the sample surface, eventually covering it entirely, accompanied by the gradual coverage of greyish-white corrosion products. During the filiform corrosion propagation, pitting corrosion initiated in areas where filaments converged. With further exposure time, the number of pits increased, and their size and depth grew.

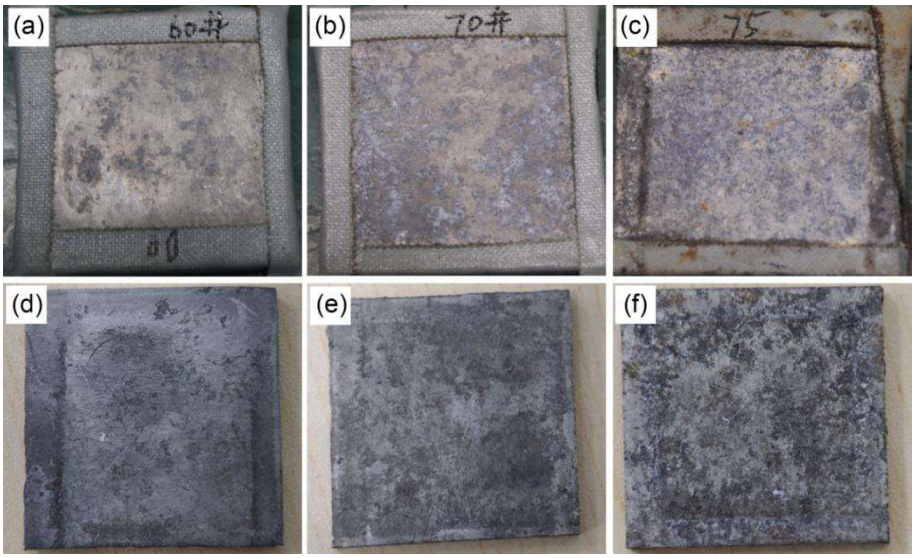


Fig. 7 Morphology of AZ91D alloy samples mounted on the chassis during PGVCT: (a)(b) 1 week; (c)(d) 4 weeks; (e)(f) 12 weeks; (a)(c)(e) before cleaning corrosion products; (b)(d)(f) after cleaning corrosion products.

The corrosion depth of AZ91D samples taken at various intervals during PGVCT was measured using the method described in Section 2.1. The statistical results are presented in Figure 8. After 12 weeks, the final average corrosion depth for the chassis-mounted AZ91D alloy was approximately 200-300 μm, with maximum pit depths reaching 400-500 μm.

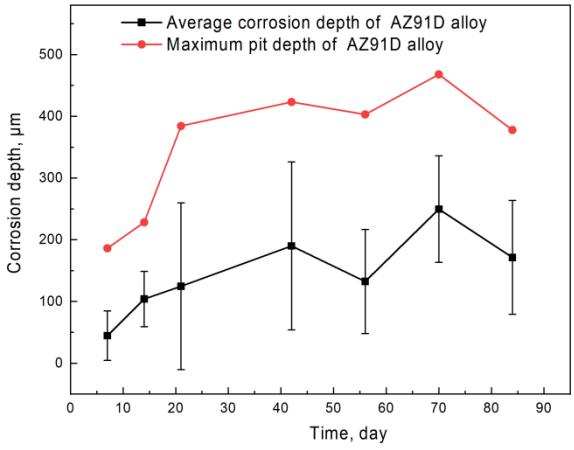


Fig. 8 Statistical results of corrosion depth for AZ91D alloy samples mounted on the chassis during PGVCT.

3.4 Corrosion rate of AZ91D alloy under laboratory conditions

AZ91D alloy samples were subjected to NSS and three cyclic corrosion test conditions (CCT 1, CCT 2, CCT 3), as in Section 2.3. Weight loss was measured at various test intervals, and

corrosion rates were calculated using formula (1). The results are shown in Fig. 9. The weight loss data for NSS showed the largest scatter, making it difficult to discern a clear trend in the corrosion rate over time. In contrast, the cyclic corrosion tests exhibited a clear decreasing trend in corrosion rate with increasing test duration, similar to the trend observed for samples mounted on the chassis during PGVCT (Fig. 6). In the initial stage of the cyclic corrosion test, the corrosion rate in terms of weight loss exceeded 1000 μm/y, and then declined to about 300 μm/y in the final stage. This value was always higher than that of the AZ91D samples mounted in the chassis area throughout PGVCT.

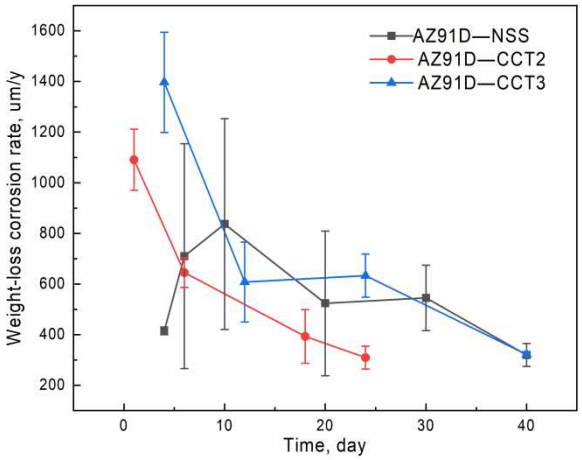


Fig. 9 Weight-loss corrosion rates of AZ91D alloy under different laboratory corrosion conditions.

The corrosion morphologies of AZ91D alloy samples after various laboratory tests are shown in Fig. 10. Both filiform corrosion and pitting were observed in all cases, but with distinct characteristics depending on the test condition. Under NSS, filiform corrosion was prominent in the initial stage, with long filaments. Later, large and deep pits formed. This condition resulted in the most severe non-uniform corrosion across the sample surface. After CCT 1, the corrosion was the mildest and most uniform. Initially, the surface was dominated by very fine filiform corrosion propagation, followed by the appearance of small, finely dispersed pits in later stages. After CCT 2, the corrosion uniformity was intermediate between NSS and CCT 1. Initial stages showed significant filiform corrosion, later transitioning to primarily small pits. After CCT 3, the initial corrosion involved finer filaments spreading across the surface, followed by the emergence of pits, with later stages characterized by increases in pit size and depth. Overall, the ranking of corrosion uniformity under different laboratory conditions was: CCT 1 > CCT 3 > CCT 2 > NSS. Comparing the corrosion morphologies from PGVCT and laboratory conditions, CCT 3 produced the closest resemblance to the chassis-mounted samples from PGVCT.

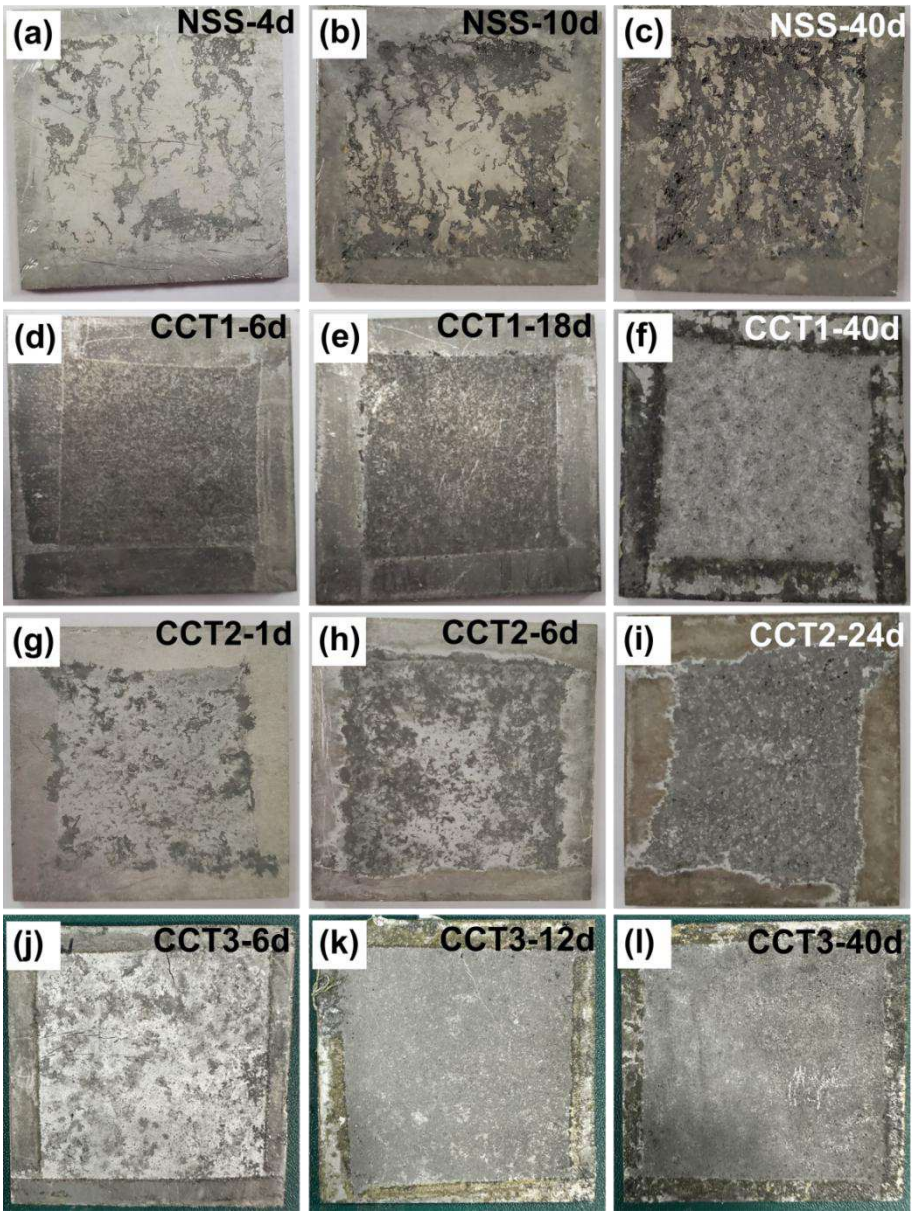


Fig. 10 Corrosion morphology of AZ91D alloy under different laboratory corrosion conditions.

Corrosion depths for samples from NSS and CCTs were measured, with statistical results shown in Fig. 11. NSS yielded the largest scatter in average corrosion depth data. After 40 days of NSS, the average corrosion depth was 300-400 μm, with maximum pit depths reaching up to 700 μm. Under CCT 1, up to 18 cycles (18 days), the average corrosion depth remained below 50 μm, and the data scatter was minimal, indicating that filament propagation was the primary corrosion mode. Beyond 18 cycles, the average corrosion depth increased rapidly, and data scatter widened, indicating the onset of pitting attack in the depth direction. After 40 cycles (40 days) of CCT 1, the average corrosion depth was 100-150 μm, with a maximum depth of about 200-300 μm. Under CCT 2, after 24 cycles (24 days), the average corrosion depth ranged from 100-150 μm, with a maximum of about 200-300 μm. Under CCT 3, after 10 cycles (40 days), the average corrosion depth was 200-300 μm, with a maximum of about 400-500 μm. Therefore, the ranking for corrosion depth under different laboratory conditions was: NSS (40 days) > CCT 3 (40 days) > CCT 2 (24 days) ≈ CCT 1 (40 days).

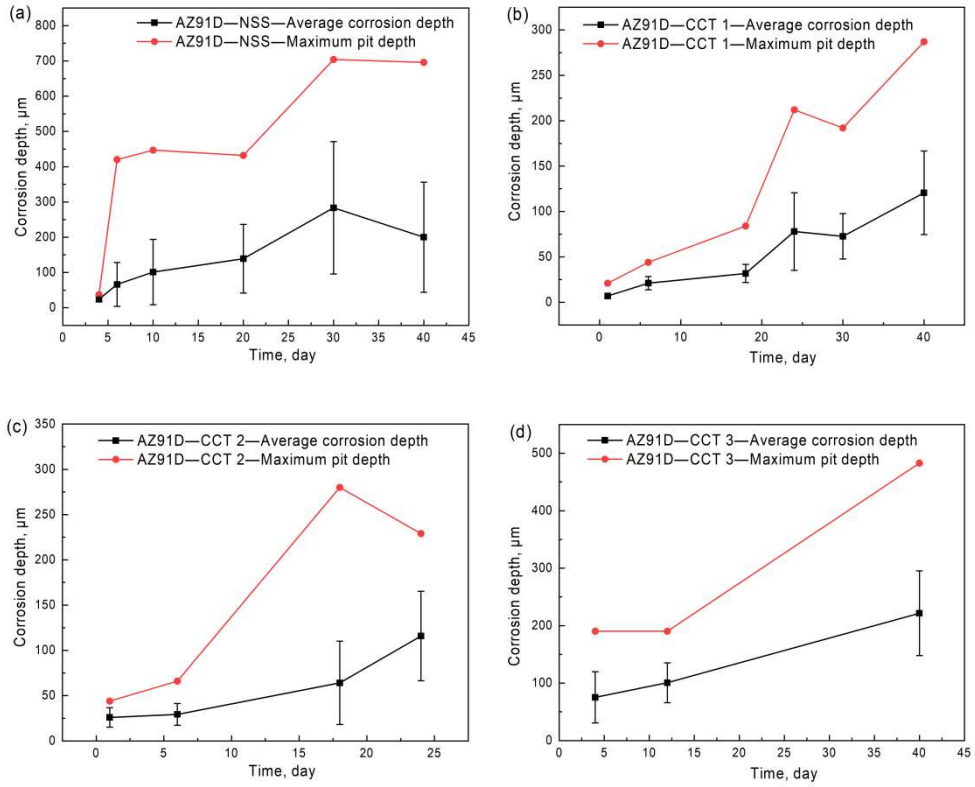


Fig. 11 Statistical results of corrosion depth for AZ91D alloy under different laboratory corrosion conditions.

4 Discussion

4.1 Microstructure evolution of AZ91D alloy during different corrosion conditions

Based on the corrosion morphology observations from PGVCT, marine transportation, and laboratory tests, the corrosion mode of AZ91D alloy consistently consists of filiform corrosion followed by pitting, as illustrated in Fig. 12. In the initial stage, filiform corrosion appears on the surface, with a depth of several tens of micrometers. Subsequently, the filaments propagate across the surface, increasing the corroded area while the depth remains at a similar level. During this stage, the measured corrosion depth data exhibit low scatter. Subsequently, pitting initiates in areas where filaments have accumulated. The pits grow both laterally and in depth, increasing the overall corrosion depth and the scatter in the data. The differences in corrosion morphology under various conditions are manifested in the size, length of filaments, and the size, depth, and uniformity of pitting.

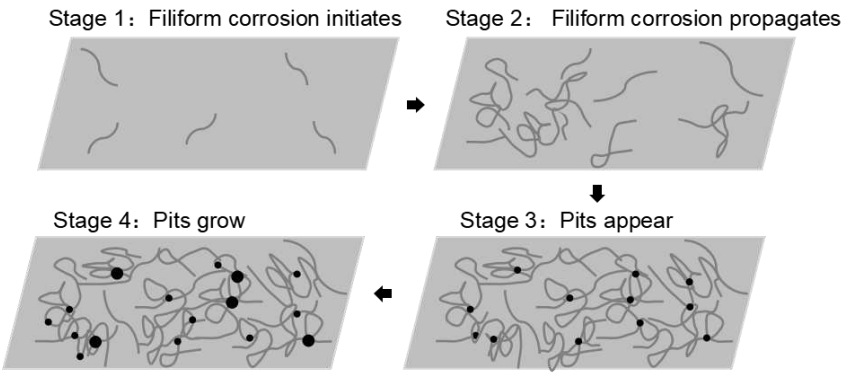


Fig. 12 Schematic diagram of the corrosion morphology evolution of AZ91D alloy.

Fig. 13(a) shows the typical microstructure of die-cast AZ91D alloy, mainly composed of dendritic α-Mg matrix and inter-dendritic β-$Mg_{17}Al_{12}$ phases. In electrolyte, micro-galvanic cells are established between the matrix and the intermetallic particles, leading to preferential corrosion of the magnesium matrix adjacent to the precipitates. Consequently, the cross-sectional corrosion morphology of the magnesium alloy exhibits pronounced features along the dendrite boundaries.

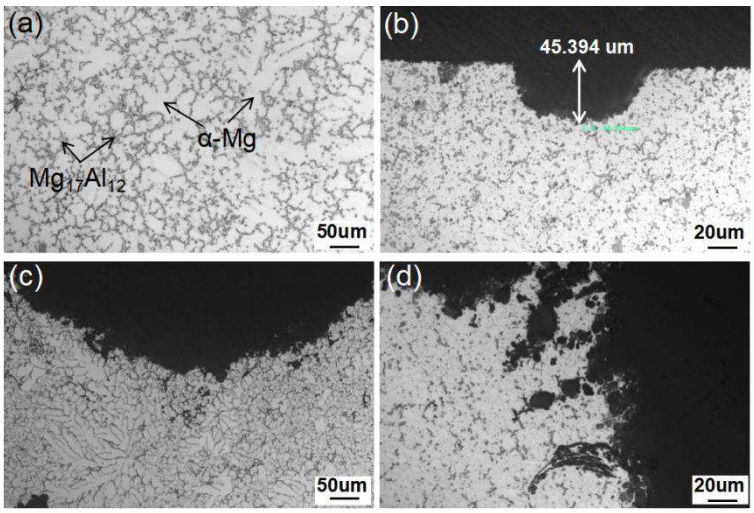


Fig. 13 Cross-sectional morphology of AZ91D alloy samples before and after corrosion: (a) Microstructure of AZ91D alloy before corrosion; (b) Cross-section morphology of filament after NSS for 4days; (c)(d) Cross-section morphology of pits after NSS for 20 days.

4.2 Filiform corrosion mechanism of AZ91D alloy

SVET was employed to measure the potential gradient caused by ionic current flow resulting from electrochemical reactions during filiform corrosion. The local current distribution in the filiform corrosion area was then calculated according to formula (3) to investigate the mechanism of filiform corrosion [13].

$$j = -\sigma\frac{\Delta E}{A} \qquad (3)$$

Where j is the local current density; σ is the electrolyte conductivity, which was tested to be 7.39 S/m for 5% NaCl solution used in this study; ΔE is the measured potential gradient; and A is the vibration amplitude of the probe.

Filiform corrosion commonly occurs on the surface of organic-coated Al alloys. It is generally understood that Al alloy filiform corrosion results from a galvanic cell consisting of an

anodic filament head, where metal dissolution occurs, and a cathodic filament tail, where the oxygen reduction reaction takes place [14]. The filament head in Al filiform corrosion typically initiates at coating defects where oxygen supply is limited. The anodic reaction at the filament head is:

$Al \rightarrow Al^{3+} + 3e^{-}$ (4)

The Al^{3+} ions undergo hydrolysis as follows:

$Al^{3+} + H_2O \rightarrow Al(OH)^{2+} + H^{+}$ (5)

This lowers the pH at the filament head, accelerating further Al dissolution, thus establishing an autocatalytic process that drives the head forward. Electrons produced at the head travel through the metal substrate to the filament tail, which is typically an oxygen-rich area, where the cathodic oxygen reduction occurs:

$O_2 + 2H_2O + 4e^{-} \rightarrow 4OH^{-}$ (6)

This raises the pH at the tail, and the resulting $Al(OH)_3$ precipitates, clogging the tail channel and rendering it inactive. The driving force for Al filiform corrosion is the oxygen concentration gradient between the filament head and tail.

In contrast to Al, uncoated Mg alloy is also susceptible to filiform corrosion. Filiform corrosion is the primary corrosion form in the early stages for Mg alloy, with filaments spreading across the surface, increasing the corroded area while the depth changes little. According to literature, the highly active chemical nature of Mg facilitates the easy formation of oxide films on its surface, thereby creating conditions suitable for the development of corrosion micro-cells. Geraint Williams [15] proposed a mechanistic model for Mg alloy filiform corrosion. The filament head acts as the anode, where Mg dissolution occurs:

$Mg \rightarrow Mg^{2+} + 2e^{-}$ (7)

Cl^{-} ions migrate into the anodic area, accelerating the Mg dissolution at the head. The filament tail serves as the cathode, where the hydrogen evolution reaction takes place, as shown in formula (1). $Mg(OH)_2$ corrosion products form at the tail, creating an inert area. Since oxygen reduction reaction is not involved, Mg filiform corrosion is independent of oxygen concentration. Its driving force is the Cl^{-} concentration gradient between the head and tail, and the availability of water for the HER. A comparison of the filiform corrosion mechanisms for Al and Mg alloys is presented in Table 2.

Table 2 Filiform corrosion mechanisms for Mg and Al alloys

	Al alloy	Mg alloy
Surface State	Organic-coated surface	Both coated and uncoated surface
Anode/Cathode	filament head serves as the anodic region where metal dissolution occurs, while filament tail acts as the cathodic region where oxygen reduction takes place.	filament head serves as the anodic region where Mg dissolution occurs, while filament tail acts as the cathodic region where hydrogen evolution takes place.
Driving Force	Oxygen concentration gradient between filament head and tail	Cl^{-} concentration gradient and H_2O availability between filament head and tail

To verify the proposed filiform corrosion mechanism, AZ91D alloy was immersed in 5% NaCl solution. The initiation and propagation of filiform corrosion were observed, and SVET mapping was performed on the filament area at different stages to obtain the local current distribution during filament generation and propagation. As shown in Fig. 14, no filiform corrosion was observed on the surface at the initial immersion stage, and the local current density was nearly zero. Upon immersion for 330 minutes, filiform corrosion began to appear, and the current density in the filament region significantly increased, reaching up to 2 A/m². With prolonged immersion, the filaments gradually expanded both upwards and downwards. The current density distributions consistently showed that the filament head always exhibited the highest current density, and this high-density region correspondingly moved upwards/downwards with the filament propagation. Finally, after 26 hours of immersion, the filament heads had propagated outside the scanned area, leaving the entire scanned region consisting of the inert filament tails. At this stage, the surface current density distribution returned to nearly zero. This observation not only confirms the proposed mechanism for AZ91D alloy filiform corrosion, but also demonstrates that filiform corrosion propagates only across Mg alloy surface without significant depth penetration.

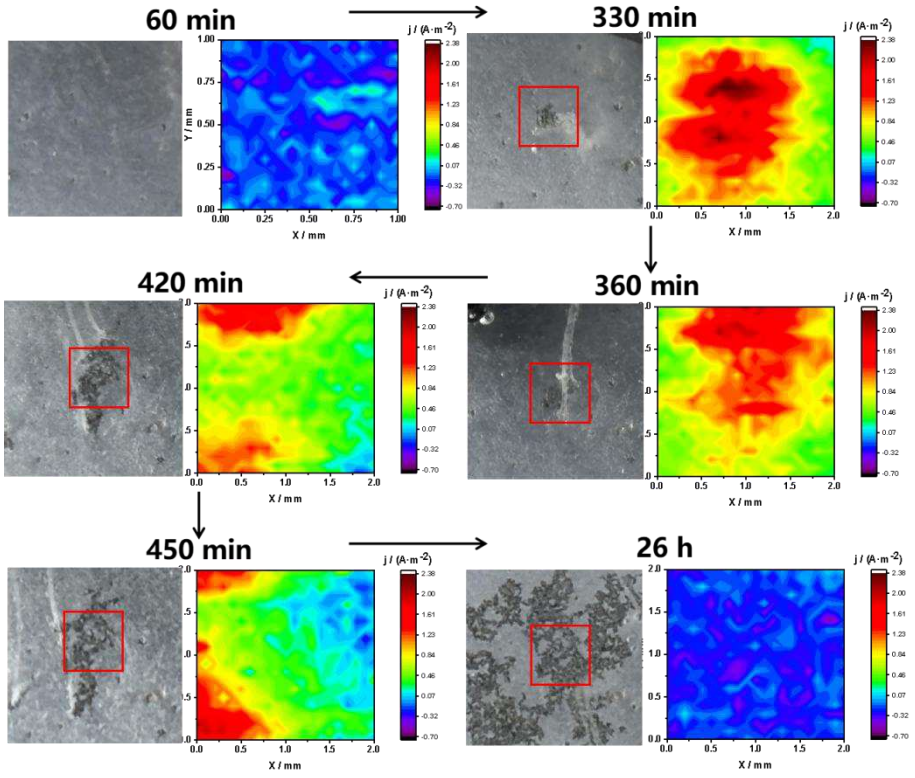


Fig. 14 Evolution of local current density distribution during the propagation of filiform corrosion on AZ91D alloy.

Since filiform corrosion is related to Cl^- concentration and water availability, environmental conditions involving salt spray and high humidity promote its development. Therefore, in laboratory settings, longer durations of salt spray and high humidity favor filiform corrosion growth. Among the four laboratory conditions used in this study, the ranking for the proportion of time spent in salt spray and high humidity was: NSS > CCT 2 > CCT 3 > CCT 1. This also explains why filiform corrosion was longest and most prominent after NSS, while it was shortest and least prominent after CCT 1.

4.3 Correspondence between atmospheric and laboratory corrosion behavior of AZ91D alloy

The corrosion process of AZ91D alloy in the atmospheric environment is illustrated in Fig. 15. In humid air, electrochemical corrosion initiates in the micro/nano-scale thin electrolyte layer on Mg surface, producing Mg^{2+} and OH^- ions. Because the liquid film is very thin, these ions quickly reach local saturation, leading to the formation of $Mg(OH)_2$ corrosion products. Subsequently, the corrosion products increase in volume and thickness, eventually protruding above the thin liquid film, effectively stopping the corrosion process in that area. During dry periods, the thin liquid film disappears, and the corrosion products formed on Mg surface tend to dry and harden. In the subsequent wet phase, areas free of corrosion products will preferentially corrode, generating new corrosion products, which then solidify during the next dry phase, ultimately resulting in a relatively uniform layer of corrosion products. In marine atmospheric environments, salt particles deposit onto Mg surface, absorbing moisture and forming a high Cl^- concentration electrolyte. Closer proximity to the coastline results in greater salt deposition, more water absorption, thicker and more extensive liquid films, and also increases the likelihood of micro-galvanic coupling between distant cathodic secondary phases and local anodic sites, thereby accelerating Mg alloy corrosion rate.

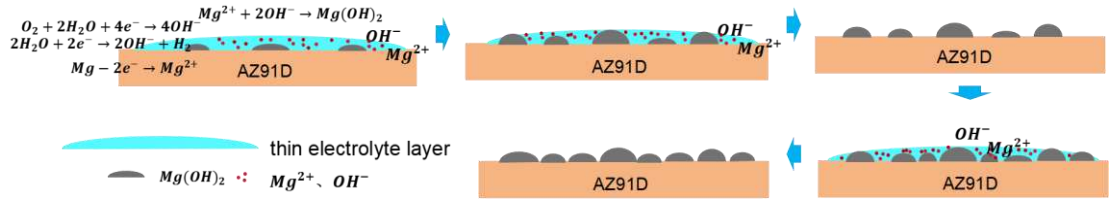


Fig. 15 Schematic diagram of the atmospheric corrosion process for AZ91D alloy.

During NSS test, however, Mg alloy is continuously exposed to high humidity and high Cl^- concentration. The liquid film thickness is about 10-100 μm, and there is no dry phase. Therefore, AZ91D alloy remains in a state of rapid corrosion. The resulting corrosion products, lacking a consolidation phase, tend to be less uniform, less dense, and offer weaker protection. This leads to excessively rapid and non-uniform corrosion rates under NSS, which deviate significantly from the behavior observed in atmospheric environments.

In CCT environments, temperature, humidity, and Cl^- concentration fluctuate cyclically. Corrosion occurs during the salt spray/high humidity phases, while the dry phases halt corrosion and allow the corrosion products to solidify. Thus, CCT exposure more closely mimics the atmospheric corrosion of Mg alloys compared to NSS. Based on the previous analysis, the proportion of time occupied by salt spray and high humidity within the overall cycle is crucial for CCTs. Thus, this proportion is defined as p (as in Equation (8) below).

$$p = \frac{T_S + T_H}{T_O} \qquad (8)$$

Where T_S represents the salt spray time within one cycle period, T_H represents the high-humidity time within one cycle period, and T_O represents the total time of one cycle.

Among the three cyclic conditions studied, p values rank as follows: CCT 2 (2/3) > CCT 3 (about 1/2) > CCT 1 (about 1/3). According to the morphology observations in Section 3.4, the ranking for corrosion uniformity under different laboratory conditions was: CCT 1 > CCT 3 > CCT 2 > NSS. Therefore, a lower p value leads to more uniform corrosion, less pronounced filiform corrosion, and smaller pits.

Among three CCT conditions, CCT 3 produced the closest resemblance in corrosion morphology to the chassis-mounted samples from PGVCT. Furthermore, comparing the corrosion depth data from Sections 3.3 and 3.4, the average corrosion depth after 10 cycles of CCT 3 and 12 weeks of PGVCT were both in the 200-300 μm range, with maximum pit depths in the 400-500 μm range. Therefore, it is concluded that the corrosion behavior of AZ91D alloy under CCT 3 condition has the best correspondence with that observed on the chassis during PGVCT.

5 Conclusions

This study investigated the corrosion behavior of AZ91D die-cast magnesium alloy under marine transportation, vehicle-grade accelerated corrosion, and various laboratory environments. The atmospheric corrosion mechanism of Mg alloy was elucidated, and the correspondence between its corrosion behavior in vehicle-grade and laboratory tests was established. The following conclusions were drawn:

(1) AZ91D alloy corrosion is primarily characterized by filiform corrosion and pitting. A comprehensive evaluation of its corrosion behavior requires the combined assessment of corrosion morphology observation and depth measurements.
(2) CCT tests provide a closer approximation to the atmospheric corrosion of AZ91D alloy. Among different CCT profiles, the proportion of time spent in salt spray and high humidity conditions is a key factor influencing the corrosion behavior of Mg alloy.
(3) The corrosion behavior of AZ91D alloy under CCT 3 condition exhibits the best correspondence with that observed on the chassis during PGVCT.

Acknowledgement

This work was financially supported by BYD Automotive Industry Co., Ltd, Automotive Engineering Research Institute, Product Technology Pre-research Project (grant numbers JGCC04).

References

[1] C.M. Yan, C. Liu, M.L. Wang, J.S. Wang, G.Y. Tian, Z.H. Yang, H. Su, C. Zhang, C.P Xue, Y.S. Miao, Q. Li, In Situ Observation of the Influence of the Corrosion Inhibitor Phases on the Corrosion Process in Mg-2RE Alloys, J. Mater. Eng. Perform. 2026, 35, p 11074-11086, doi: 10.1007/s11665-025-12522-6.

[2] X.H. Shen, S.Q. Ma, S.R. He, Y.L. Shi, N. Xu, S.H. Pan, Electrochemistry-Informed Surface Engineering by Ultrasonic Burnishing for Improved Corrosion Resistance in AZ91D Mg Alloy, J. Mater. Eng. Perform. 2026, 35, p 27692-27709, doi: 10.1007/s11665-026-13649-w

[3] M. Esmaily, J.E. Svensson, S. Fajardo, N. Birbilis, G.S. Frankel, S. Virtanen, R. Arrabal, S. Thomas, L.G. Johansson, Fundamentals and advances in magnesium alloy corrosion, Prog. Mater. Sci. 89 (2017), p 92-193, doi: 10.1016/j.pmatsci.2017.04.011.

[4] A.D. King, N. Birbilis, J.R. Scully, Accurate electrochemical measurement of magnesium corrosion rates: A combined impedance, mass-loss and hydrogen collection study, Electrochim. Acta. 121 (2014), p 394-406, doi: 10. 1016/j.electacta.2013.12.124.

[5] J.F. Huang, G.L. Song, Y.X. Zhu, D.J. Zheng, Z.M. Wang, The anodically polarized Mg surface products and accelerated hydrogen evolution, J. Magnes. Alloy. 11 (2023), p 230-248, doi:

10.1016/j.jma. 2021.05.008.
[6] C.L. Guo, Q.F. Zheng, AZ31 镁合金在海洋大气环境中的腐蚀行为 (Corrosion behavior of AZ31 magnesium alloy in marine atmospheric environment), Chin. J. Rare Met. 2013(37), p 21-26, (In Chinese) doi: 10. 3969/j. issn. 0258-7076. 2013.01.004.
[7] P. Gong, X.J. Cao, S.Q. Ning, L.P. Zhu,不同环境对 AZ61 镁合金大气腐蚀的影响 (Effects of different environments on atmospheric corrosion of AZ61 magnesium alloy), China Surf. Eng. 2015(28), p 123-128, (In Chinese) doi: 10. 11933/j. issn. 1007-9289. 2015.05.019.
[8] J.Y. Li, AZ91D 镁合金在冷却液及大气环境中的腐蚀研究 (Corrosion study of AZ91D magnesium alloy in coolant and atmospheric environments), Master's Thesis. Taiyuan University of Science and Technology. 2009, (In Chinese)
[9] L.J. Yang, AZ91D 镁合金显微组织对其在特定环境下腐蚀行为的影响 (Effect of microstructure of AZ91D magnesium alloy on its corrosion behavior in specific environments), Ph.D. Dissertation. Taiyuan University of Technology. 2010, (In Chinese)
[10] Q.T. Jiang, D.Z. Lu, N. Wang, X.T. Wang, J. Zhang, J.Z. Duan, B.R. Hou, The corrosion behavior of Mg–Nd binary alloys in the harsh marine environment, J. Magnes. Alloys, 2021, 9(1), p 292-304, doi: 10.1016/j.jma.2019.12.010.
[11] J. Martin, P. Dan, L. Christofer, Atmospheric corrosion of field-exposed magnesium alloy AZ91D, Corros. Sci. 50 (2008), p 1406–1413, doi: 10.1016/j.corsci.2007.12.005.
[12] J.S. Liao, M. Hotta, S. Motoda, T. Shinohara, Atmospheric corrosion of two field-exposed AZ31B magnesium alloys with different grain size. Corros. Sci. 71 (2013), p 53–61, doi: 10.1016/j.corsci.2013.02.003.
[13] K. B. Deshpande, Experimental investigation of galvanic corrosion: Comparison between SVET and immersion techniques, Corros. Sci. 52 (2010), p 2819-2826, doi: 10.1016/j.corsci.2010.04.023.
[14] Z. Chen, H.Z. Li, X.P. Liang, M.C. Zhao, K.L. Zhang, A. Atrens, In-situ observation on filiform corrosion propagation and its dependence on Zr distribution in Mg alloy WE43, J. Magnes. Alloys, 11 (2023), p 4282-4300, doi: 10.1016/j.jma.2022.09.033.
[15] G. Williams, R. Grace, Chloride-Induced Filiform Corrosion of Organic-Coated Magnesium.Electrochim. Acta, 56 (2011), p 1894-1903, doi: 10.1016/j.electacta.2010.09.005.